

4D Cloud Scattering Tomography Supplementary Material

Roi Ronen, Yoav Y. Schechner
Viterbi Faculty of Electrical & Computer Eng.
Technion - Israel Institute of Technology
Haifa, Israel

ronen.roi@gmail.com
yoav@ee.technion.ac.il

Eshkol Eytan
Department of Earth & Planetary Sciences
The Weizmann Institute of Science
Rehovot, Israel

eshkol.eytan@weizmann.ac.il

Abstract

This is a supplementary document to the main manuscript. Here we provide more numerical results. Moreover, this document details pre-processing of real world data, which is presented in section 7 of the main manuscript. Additionally, we elaborate about the computational complexity of the method, give evaluation for the Gaussian weights that were used in the main manuscript and an interpretation using a hidden field for the iterative procedure described in section 5.1 of the main manuscript.

1. Outline

This supplementary material contains five parts. The first part (Sec. 2) elaborates on pre-processing which is applied to real world measurements, presented in Sec. 7 of the main manuscript. This data was collected by the AirMSPI instrument. The second part, Sec. 3, provides an additional example of the temporal auto-correlation of cloud microphysics and more simulation results which were not included in the main manuscript, for space limits. The third part (Sec. 4) analyzes the computational complexity of our proposed method. In Sec. 5, we give an interpretation for the iterative procedure described in Sec. 5.1 of the main manuscript using a hidden field representation. Sec. 6 provides an evaluation for the Gaussian weights that were used in Sec. 5.1 of the main manuscript.

2. Pre-processing Real World Data

The main manuscript presents results using real world measurements. The data were acquired by the AirMSPI instrument. As explained in Sec. 7 of the main manuscript, while AirMSPI flies, clouds move due to wide-scale wind

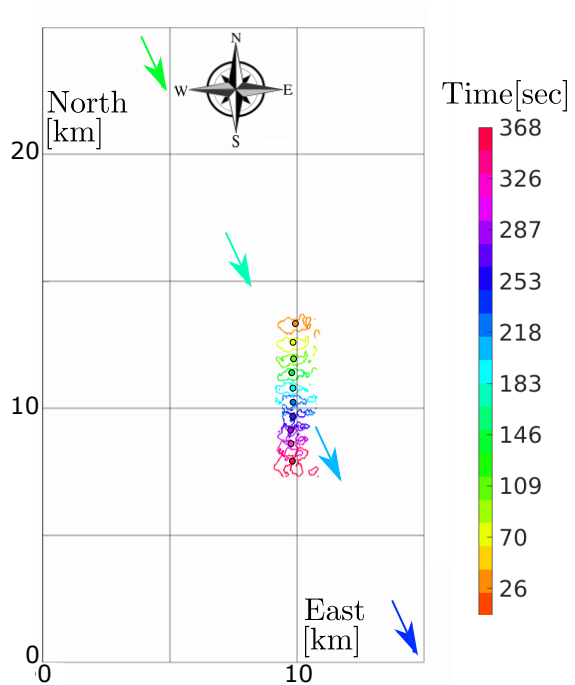


Figure 1. Geometry of the AirMSPI real world setup which led to the data presented in Sec. 7 of the main manuscript. The color represents the locations of the cloud and the AirMSPI instrument in the different time states. The cloud's outer contour and its corresponding center of mass, marked in a circle, are presented per state. The AirMSPI location and velocity are marked by arrows. The arrows point to the AirMSPI flight direction azimuth of 154° relative to the North. Due to the domain size, not all AirMSPI locations are illustrated here. Due to wind, the cloud moves at 57 km/h in azimuth 182° relative to the North.

at their altitude. The geometry of AirMSPI's path and the cloud drift during the experiment is presented in Fig. 1 above. In order to eliminate the influence of wide-scale

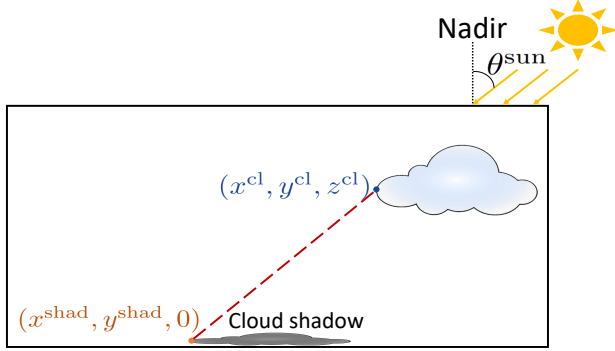


Figure 2. Illustration of estimation of the cloud altitude using a shadow.

wind, a registration process of the cloud images is done. Moreover, for tomographic recovery, we need to have an assessment of the Earth surface albedo, under the clouds. This section describes how pre-processing estimates the wind and albedo.

2.1. Wind Estimation

Clouds are segmented from the surface automatically [12]. Cloudy pixels are then used to estimate the cloud center of mass in each image [7]. A registration of these centers of mass can be done by triangulation. However, triangulation of images of a moving object using a translating camera has an inherent ambiguity. This ambiguity can be solved if the cloud height is known. In this work, we assess this altitude of a cloud by its shadow [1, 6, 8]. Let (x^{cl}, y^{cl}, z^{cl}) and $(x^{shad}, y^{shad}, 0)$ be a point on a cloud and its corresponding shadow point on the earth surface, respectively (see Fig. 2 above). Let $\varrho^{shad} = \sqrt{(x^{cl} - x^{shad})^2 + (y^{cl} - y^{shad})^2}$. We obtain x^{cl}, y^{cl}, x^{shad} and y^{shad} from the AirMSPI images. Given the solar zenith angle relative to the nadir θ^{sun} , the altitude z^{cl} satisfies

$$z^{cl} = \frac{\varrho^{shad}}{\tan(\theta^{sun})}. \quad (1)$$

For the example shown in Sec. 7 of the main manuscript, we estimated the cloud base height as ≈ 500 m and its top at ≈ 1100 m. Indeed taking MODIS/AQUA [2] retrievals of cloud top heights, indicate that the clouds' top in the region¹ does not exceed 1000 m, which makes our approximation reasonable.

We approximate the cloud horizontal velocity by back-projecting the images from the locations of the cameras to the altitude of z^{cl} . From the center of mass of these back-projections, we assess the velocity. We register the camera locations so the projections of the center of mass of all images intersect at the same point at altitude of z^{cl} . The im-

¹This data applies over the coast of California, 38N 122W, on Feb/03/2013 at 13:30 local time.

ages and the new locations of the camera are the input for the 4D tomographic recovery.

2.2. Surface Albedo Estimation

3D radiative transfer calculations require the surface albedo. We use non-cloudy pixels to estimate the albedo. Let \mathcal{Y} be a set of non-cloudy pixels. We estimate the surface albedo a^{ground} as,

$$\hat{a}^{ground} = \operatorname{argmin}_a \sum_{y \in \mathcal{Y}} \|y - \mathcal{F}(\beta^{air}; a)\|_2^2, \quad (2)$$

where β^{air} represents the extinction coefficient of air in 3D with no clouds. Here $\mathcal{F}(\beta^{air}; a)$ is a rendering (forward) model, where the surface albedo is set to be a . That is, sunlight interacts only with the air and the surface. Scattering by air is assumed to be known [5, 13]. The optimization problem is solved by the Brent minimization method [3], implemented by the SciPy package [11]. For the example shown in Sec. 7 of the main manuscript, the surface albedo is estimated to be 0.04.

3. Additional Simulations

3.1. Cloud Temporal Spectrum

Sec. 3 of the main manuscript indicates that the correlation time of a convective cloud at 10 sec resolution is about 20 to 50 seconds. Thus, a temporal sampling period of 30 sec or shorter is required. We assess this in an additional cloud simulation. We conducted a single cloud simulation in high resolution, using small changes, relative to the simulation described in Sec. 6 of the main manuscript. The simulation parameters and setting are similar. However, the perturbation that initiates the convection and turbulent flow has a smaller horizontal size. This creates a smaller cloud with a horizontal width of ≈ 400 m. This cloud is more sensitive to mixing and evaporation than the cloud in the main manuscript whose width is ≈ 800 m. Because mixing with the environment is more intense here, the clouds' growth is inhibited. It cannot exceed a height of 1400 m, compared to a 2000 m ceiling of the cloud in the main manuscript.

Using the same process described in Sec. 3 of the main manuscript, the temporal auto-correlation functions of \mathcal{L}_t and horizontally-averaged r_t^e are presented in Fig. 3[Top] in the next page. The auto-correlation function of r_t^e behaves similarly to that of v_t^e . Here the required temporal sampling period is more tolerable compared to the presented temporal sampling period in the main manuscript.

3.2. Additional Tomography Results

Recall that our method is demonstrated on two simulated clouds, *Cloud (i)* and *Cloud (ii)*, using several types of imaging setups: Setup A, Setup B and Baseline.

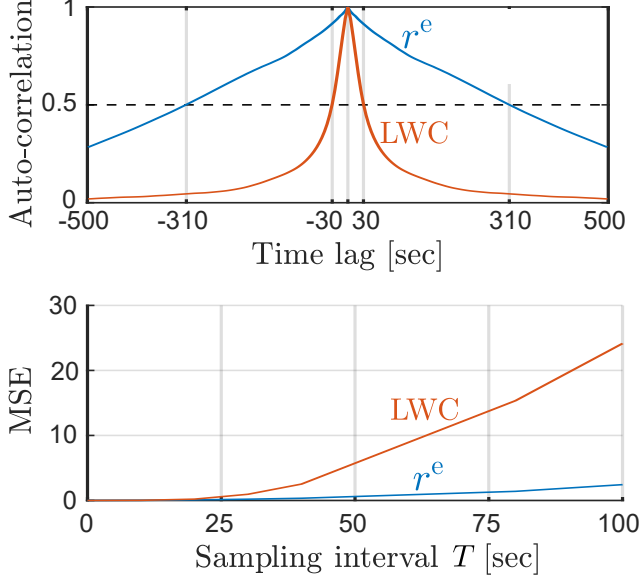


Figure 3. [Top] Auto-correlation of cloud field microphysics. The auto-correlation of LWC and r^e decreases to 0.5 after 30 sec and 310 sec, respectively. [Bottom] MSE (Eq. 13 in the main manuscript) of LWC and r^e .

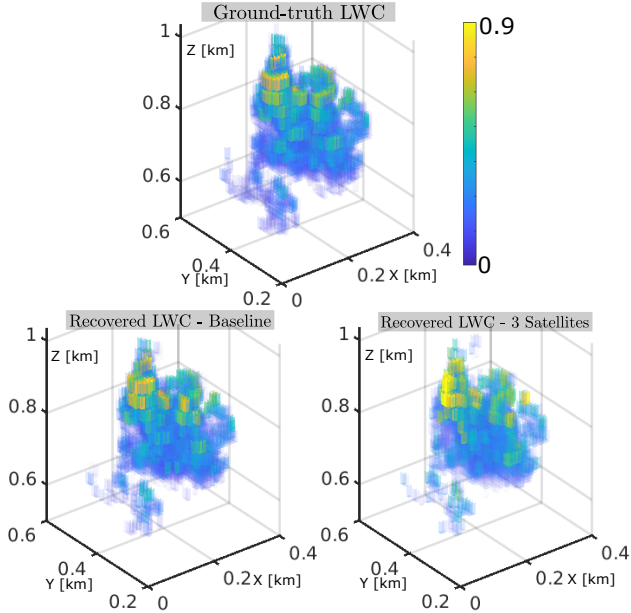


Figure 4. *Cloud (ii)*. Results of recovery by the Baseline and Setup A are compared to the ground-truth.

Fig. 4 above presents the 3D tomographic results of *Cloud (ii)* at $t = (t_1 + t_{N^{\text{state}}})/2$ using Setup A. The recovery used $\sigma = 20$ sec. Moreover, recall the error measures as Eq. (19) defined in the main manuscript. Fig. 5 above presents $\varepsilon_t, \varepsilon$ for *Cloud (ii)*. It reinforces the assessment that a value $\sigma \sim 20$ sec is natural, as explained in Sec. 3 of the main manuscript.

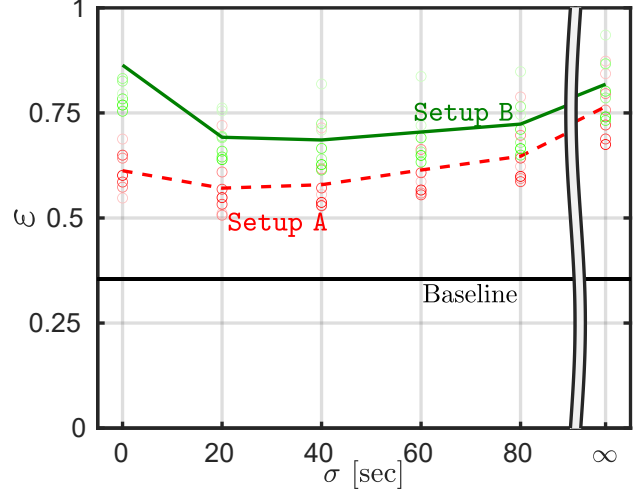


Figure 5. *Cloud (ii)*. The errors ε_t in the main manuscript are marked by colored circles, whose saturation decays the farther the sampling time is from $(t_1 + t_{N^{\text{state}}})/2$. The measure ε in the main manuscript is marked by solid or dashed lines, with corresponding colors. The setting $\sigma = \infty$ refers to the solution by the state of the art, i.e. 3D static scattering tomography.

	$\sigma = 20$ sec	$\sigma = 60$ sec	$\sigma = \infty$
Setup A	0.45	0.55	0.64
Setup B	0.6	0.66	0.74
Setup C	0.79	0.74	0.9

Table 1. The error ε_t in the main manuscript at $t = (t_1 + t_{N^{\text{state}}})/2$ of *Cloud (i)*, when $T = 10$ sec. The state of the art 3D static CT complies with $\sigma = \infty$.

Figs. 6 and 7 in the next page respectively visualize the results of *Cloud (i)* and *Cloud (ii)*. The 3D cut-sections of the error $|\mathcal{L}_t^{\text{true}}(\mathbf{x}) - \hat{\mathcal{L}}_t(\mathbf{x})|$ at $t = (t_1 + t_{N^{\text{state}}})/2$ are presented for Setup A, Setup B and Baseline in Figs. 6 and 7[Top]. Fig. 7[Bottom] uses scatter plots to compare the ground-truth to the results obtained by either the Baseline, Setup A or Setup B. Also, we compare the recovery results at $t = (t_1 + t_{N^{\text{state}}})/2$ quantitatively for the three setups in Table 1 above.

4. Computational Complexity

Sec. 5.1 of the main manuscript introduces an iterative procedure for 4D CT estimation of cloud LWC

$$\mathcal{L}_t(k+1) = \mathcal{L}_t(k) - \eta \mathbf{g}_t[\mathcal{B}(k)], \quad (3)$$

where

$$\mathbf{g}_t(\mathcal{B}) = \sum_{t' \in \mathcal{T}} w_t(t'|\sigma) \frac{\partial \mathcal{F}(\mathcal{L}_{t'})}{\partial \mathcal{L}_{t'}} [\mathcal{F}(\mathcal{L}_{t'}) - \mathbf{y}_{t'}]. \quad (4)$$

The time complexity for solving Eqs. (3,4) above is governed by the gradient calculation $\mathbf{g}_t(\mathcal{B})$. Computing the Ja-

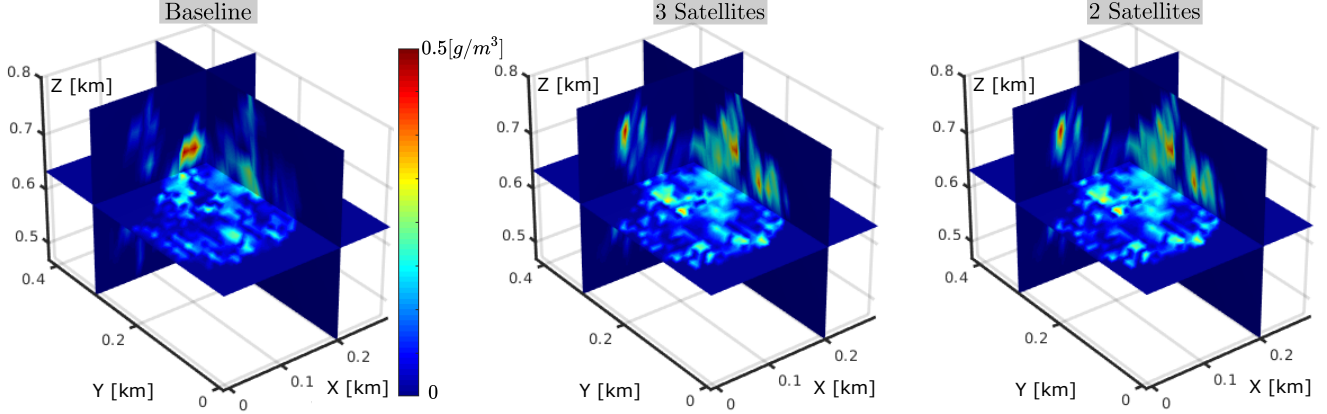


Figure 6. *Cloud (i)*. 3D cut-sections of the error $|\mathcal{L}_t^{\text{true}}(\mathbf{x}) - \hat{\mathcal{L}}_t(\mathbf{x})|$ at $t = (t_1 + t_{N^{\text{state}}})/2$ for Baseline, Setup A and Setup B.

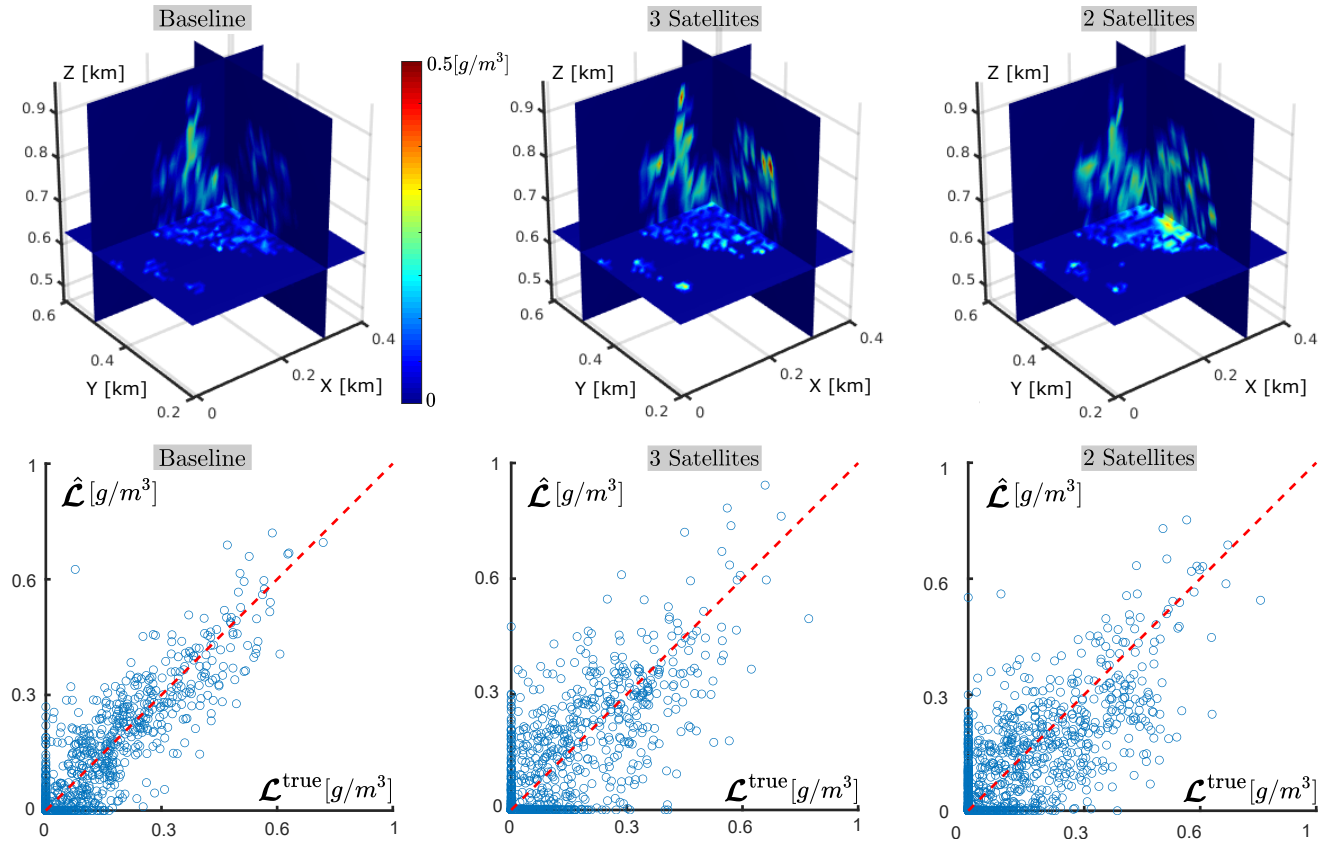


Figure 7. *Cloud (ii)* comparison for Baseline, Setup A and Setup B. [Top] 3D cut-sections of the error $|\mathcal{L}_t^{\text{true}}(\mathbf{x}) - \hat{\mathcal{L}}_t(\mathbf{x})|$ at $t = (t_1 + t_{N^{\text{state}}})/2$. [Bottom] Scatter plots that use randomly selected 20% of the data points, for display clarity. The Baseline, Setup A and Setup B scatter plot correlations are 0.92, 0.82 and 0.78, respectively.

cobian $\partial \mathcal{F}(\mathcal{L}_{t'}) / \partial \mathcal{L}_{t'}$ in Eq. (4) is complex, thus it is established numerically by a surrogate function that evolves through iterations [7, 9]. Calculating the gradient includes two dominant time-consuming processes that are executed in alternation. The first process calculates the forward model for the N^{state} cloud states $\{\mathcal{F}(\mathcal{L}_{t'})\}_{t' \in \mathcal{T}}$. The

second process sums over the entire set of measurements, which does not depend on the number of cloud states that we seek to recover.

A spherical harmonic discrete ordinate method (SHDOM) code is used for computing the numerical forward model $\mathcal{F}(\cdot)$ and the Jacobian. SHDOM iteratively

updates the estimation of 3D radiation fields until convergence. Calculating the forward model for the N^{state} cloud states can be done in parallel. Thus, the time complexity is governed by the temporal state, for which the SHDOM forward model code takes the longest time to compute. By calculating the forward model for all cloud states in parallel, the time complexity of gradient calculation is insensitive to the number of cloud states N^{state} . Algorithm 1 is a pseudo-code of our algorithm. The source code is publicly available at [10].

Algorithm 1 4D Cloud Scattering Tomography

Require: $\{\mathbf{y}_{t'}\}_{t' \in \mathcal{T}}$ and $\sigma \geq 0$
 $\mathcal{B}(0) = \{\mathcal{L}_{t'} = 0.01\}_{t' \in \mathcal{T}}$
 $k = 0$
repeat
 Calculate $\{\mathcal{F}[\mathcal{L}_{t'}(k)]\}_{t' \in \mathcal{T}}$ ▷ In parallel
 Approximate $\left\{\frac{\partial \mathcal{F}}{\partial \mathcal{L}_{t'}}[\mathcal{L}_{t'}(k)]\right\}_{t' \in \mathcal{T}}$ ▷ Ref. [7]
 Calculate $\{\mathbf{g}_{t'}[\mathcal{B}(k)]\}_{t' \in \mathcal{T}}$ ▷ Eq. (4)
 $\forall t \in \mathcal{T}$ update $\mathcal{L}_t(k+1)$ ▷ Eq. (3)
 $k = k + 1$
until converge $\{\mathbf{y}_{t'} \approx \mathcal{F}[\mathcal{L}_{t'}(k)]\}_{t' \in \mathcal{T}}$

As a numerical example, we used 20 iterations of the L-BFGS-B optimization. Using measurements of *Cloud (i)* acquired by Setup A, the run-time of the solution by our method was 501 sec. The static solution took 301 sec. In both, the computer was Intel® Xeon® Gold 6240 CPU @ 2.60GHz with 72 cores. Although our method recovers $N^{\text{state}} = 7$ times more voxels, the run-time is less than twice that of the static solution. The time difference is caused by overheads of saving and loading larger data with our method, and nonoptimal task division for the cores.

5. Cost on a Hidden Field

In this section, we present an interpretation for the iterative procedure of solving the problem of 4D CT estimation of cloud LWC (Eqs. 3,4 above). Recall that Eq. (18) in the main manuscript defines $w_t(t'|\sigma)$ as Gaussian weights

$$w_t(t'|\sigma) = s \exp\left(-\frac{|t-t'|^2}{2\sigma^2}\right), \quad (5)$$

where s is a normalization factor. Let $w_t(t'|\tilde{\sigma})$ be Gaussian weights with variance $\tilde{\sigma}^2$. Suppose the cloud LWC can be represented by

$$\mathcal{L}_t[\mathcal{B}^{\text{hidden}}] = \sum_{t' \in \mathcal{T}} w_t(t'|\tilde{\sigma}) \mathcal{L}_{t'}^{\text{hidden}}, \quad (6)$$

where $\mathcal{L}_t^{\text{hidden}}$ is a hidden representation at time t and $\mathcal{B}^{\text{hidden}} = \{\mathcal{L}_{t'}^{\text{hidden}}\}_{t' \in \mathcal{T}}$. The set $\mathcal{B}^{\text{hidden}}$ is equivalent

to the set $\mathcal{B} = \{\mathcal{L}_t\}_{t \in \mathcal{T}}$ through a linear transformation having Gaussian weights. Let us formulate 4D CT using the hidden field representation

$$\hat{\mathcal{B}}^{\text{hidden}} = \underset{\mathcal{B}^{\text{hidden}}}{\operatorname{argmin}} \sum_{t \in \mathcal{T}} \mathcal{E}[\mathbf{y}_t, \mathcal{F}(\mathcal{B}^{\text{hidden}})]. \quad (7)$$

Recall that \mathbf{y}_t , the measurements acquired at time t , depends explicitly only on the cloud state at this time, \mathcal{L}_t . Thus,

$$\mathcal{E}[\mathbf{y}_t, \mathcal{F}(\mathcal{B}^{\text{hidden}})] = \frac{1}{2} \|\mathbf{y}_t - \mathcal{F}(\mathcal{L}_t[\mathcal{B}^{\text{hidden}}])\|_2^2. \quad (8)$$

Eq. (7) above can be solved efficiently by gradient-based methods. The gradient of Eq. (7) above is

$$\frac{\partial}{\partial \mathcal{L}_t^{\text{hidden}}} \sum_{t' \in \mathcal{T}} \mathcal{E}[\mathbf{y}_t, \mathcal{F}(\mathcal{B}^{\text{hidden}})] = \sum_{t' \in \mathcal{T}} \frac{\partial \mathcal{E}[\mathbf{y}_{t'}, \mathcal{F}(\mathcal{L}_{t'})]}{\partial \mathcal{L}_{t'}} \frac{\partial \mathcal{L}_{t'}}{\partial \mathcal{L}_t^{\text{hidden}}}. \quad (9)$$

From Eq. (8) above,

$$\frac{\partial \mathcal{E}[\mathbf{y}_{t'}, \mathcal{F}(\mathcal{L}_{t'})]}{\partial \mathcal{L}_{t'}} = \frac{\partial \mathcal{F}(\mathcal{L}_{t'})}{\partial \mathcal{L}_{t'}} [\mathcal{F}(\mathcal{L}_{t'}) - \mathbf{y}_{t'}], \quad (10)$$

while from Eq. (6) above,

$$\frac{\partial \mathcal{L}_{t'}}{\partial \mathcal{L}_t^{\text{hidden}}} = w_t(t'|\tilde{\sigma}). \quad (11)$$

From Eqs. (9,10,11) above, for optimizing problem (7) above, the gradient is

$$\mathbf{g}_t^{\text{hidden}}(\mathcal{B}) = \sum_{t' \in \mathcal{T}} w_t(t'|\tilde{\sigma}) \frac{\partial \mathcal{F}(\mathcal{L}_{t'})}{\partial \mathcal{L}_{t'}} [\mathcal{F}(\mathcal{L}_{t'}) - \mathbf{y}_{t'}]. \quad (12)$$

A gradient-based approach then performs per iteration k :

$$\mathcal{L}_t^{\text{hidden}}(k+1) = \mathcal{L}_t^{\text{hidden}}(k) - \eta \mathbf{g}_t^{\text{hidden}}[\mathcal{B}(k)] \quad (13)$$

where η is a step size. Every iteration, $\mathcal{B}(k)$ is updated by Eq. (6) above,

$$\mathcal{L}_t(k+1) = \sum_{t' \in \mathcal{T}} w_t(t'|\tilde{\sigma}) \mathcal{L}_{t'}^{\text{hidden}}(k+1). \quad (14)$$

Substitute Eq. (13) above into Eq. (14) above,

$$\mathcal{L}_t(k+1) = \mathcal{L}_t(k) - \eta \sum_{t' \in \mathcal{T}} w_t(t'|\tilde{\sigma}) \mathbf{g}_{t'}^{\text{hidden}}[\mathcal{B}(k)]. \quad (15)$$

Now, we use the approximation

$$w_t(t'|\sigma) \approx \sum_{t'' \in \mathcal{T}} w_t(t''|\tilde{\sigma}) w_{t'}(t''|\tilde{\sigma}), \quad (16)$$

where

$$\sigma = \sqrt{2}\tilde{\sigma}. \quad (17)$$

We explain the approximation in Eq. (16) above using properties of continuous Gaussian PDFs, as we now explain. Let $f_\mu(\xi|\tilde{\sigma})$ and $f_{\mu'}(\xi|\tilde{\sigma})$ be two Gaussian PDFs with variance $\tilde{\sigma}^2$ and respective expectations μ and μ' . Being a PDF,

$$\int_{-\infty}^{\infty} f_{(\mu+\mu')/2}(\xi|\tilde{\sigma}/\sqrt{2}) d\xi = 1. \quad (18)$$

From [4],

$$f_\mu(\xi|\tilde{\sigma})f_{\mu'}(\xi|\tilde{\sigma}) = f_\mu(\mu'|\sqrt{2}\tilde{\sigma})f_{(\mu+\mu')/2}(\xi|\tilde{\sigma}/\sqrt{2}). \quad (19)$$

From Eq. (18) above,

$$\begin{aligned} f_\mu(\mu'|\sqrt{2}\tilde{\sigma}) &= f_\mu(\mu'|\sqrt{2}\tilde{\sigma}) \int_{-\infty}^{\infty} f_{(\mu+\mu')/2}(\xi|\tilde{\sigma}/\sqrt{2}) d\xi \\ &= \int_{-\infty}^{\infty} f_\mu(\mu'|\sqrt{2}\tilde{\sigma})f_{(\mu+\mu')/2}(\xi|\tilde{\sigma}/\sqrt{2}) d\xi. \end{aligned} \quad (20)$$

From Eqs. (19,20) above,

$$f_\mu(\mu'|\sqrt{2}\tilde{\sigma}) = \int_{-\infty}^{\infty} f_\mu(\xi|\tilde{\sigma})f_{\mu'}(\xi|\tilde{\sigma}) d\xi. \quad (21)$$

Discretizing the integral of Eq. (21) above, an approximate finite sum yields Eq. (16) above.

Substitute Eq. (16) above into Eq. (4) above

$$\begin{aligned} \mathbf{g}_t(\mathcal{B}) &\approx \\ &\sum_{t' \in \mathcal{T}} \sum_{t'' \in \mathcal{T}} w_t(t''|\tilde{\sigma})w_{t'}(t''|\tilde{\sigma}) \frac{\partial \mathcal{F}(\mathcal{L}_{t'})}{\partial \mathcal{L}_{t'}} [\mathcal{F}(\mathcal{L}_{t'}) - \mathbf{y}_{t'}]. \end{aligned} \quad (22)$$

Swap the summation order of Eq. (22) above:

$$\begin{aligned} \mathbf{g}_t(\mathcal{B}) &\approx \\ &\sum_{t'' \in \mathcal{T}} w_t(t''|\tilde{\sigma}) \sum_{t' \in \mathcal{T}} w_{t'}(t''|\tilde{\sigma}) \frac{\partial \mathcal{F}(\mathcal{L}_{t'})}{\partial \mathcal{L}_{t'}} [\mathcal{F}(\mathcal{L}_{t'}) - \mathbf{y}_{t'}]. \end{aligned} \quad (23)$$

Substitute Eq. (12) above into Eq. (23) above and use the property that $w_{t'}(t''|\tilde{\sigma}) = w_{t''}(t'|\tilde{\sigma})$. This yields,

$$\mathbf{g}_t(\mathcal{B}) \approx \sum_{t'' \in \mathcal{T}} w_t(t''|\tilde{\sigma}) \mathbf{g}_{t''}^{\text{hidden}}(\mathcal{B}). \quad (24)$$

Substituting Eq. (24) above into Eq. (15) above yields the iteration move in Eq. (3) above

$$\begin{aligned} \mathcal{L}_t(k+1) &\approx \mathcal{L}_t(k) - \eta \sum_{t' \in \mathcal{T}} w_t(t'|\tilde{\sigma}) \mathbf{g}_{t'}^{\text{hidden}}[\mathcal{B}(k)] \\ &= \mathcal{L}_t(k) - \eta \mathbf{g}_t[\mathcal{B}(k)]. \end{aligned} \quad (25)$$

Thus, the iterative procedure for 4D CT estimation in the main manuscript (Eqs. 3,4 above) can be interpreted as solving Eq. (7) above.

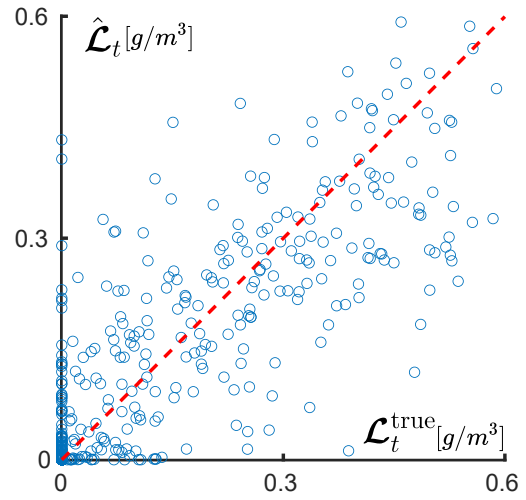
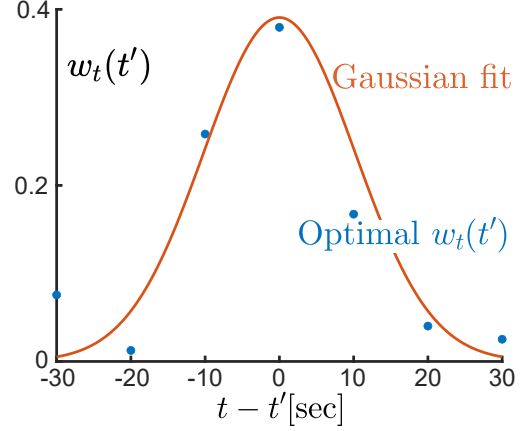


Figure 8. [Top] Optimal $w_t(t')$ are presented in blue circles and their Gaussian fit in red line. [Bottom] Comparison of true \mathcal{L}_t and $\hat{\mathcal{L}}_t$ by a scatter plot.

6. Kernel Assessment for Cloud Tomography

Recall Eq. (11) in the main manuscript,

$$\beta_t \sim \sum_{t'} w_t(t'|T) \beta_{t'}^{\text{sample}}. \quad (26)$$

We now assess the approximation of using cropped Gaussian as the kernel $w_t(t'|T)$ for recovering cloud LWC. In tomography, we do not have direct sampling of the $\mathcal{L}_{t'}^{\text{sample}}$ at time $t' \in \mathcal{T}$. We only have projected images. Let $\tilde{\mathcal{L}}_{t'}$ be the tomographic recovery of the LWC using only measurements acquired at time t' . We approximate $\mathcal{L}_{t'}^{\text{sample}} \approx \tilde{\mathcal{L}}_{t'}$. Hence instead of Eq. (26) above, suppose we approximate \mathcal{L}_t as

$$\hat{\mathcal{L}}_t(\{w_t(t')\}_{t' \in \mathcal{T}}) \approx \sum_{t' \in \mathcal{T}} w_t(t') \tilde{\mathcal{L}}_{t'}. \quad (27)$$

Let us seek the optimal set of weights $\{w_t(t')\}_{t' \in \mathcal{T}}$ by

$$\{\hat{w}_t(t')\}_{t' \in \mathcal{T}} = \underset{\{w_t(t')\}_{t' \in \mathcal{T}}}{\operatorname{argmin}} \|\mathcal{L}_t - \tilde{\mathcal{L}}_t(\{w_t(t')\}_{t' \in \mathcal{T}})\|_2^2. \quad (28)$$

Fig. 8[Top] herein shows the optimal $w_t(t')$. The plot shows that the weights are approximately Gaussian. Fig. 8[Bottom] herein shows a scatter plot of $\hat{\mathcal{L}}_t$ vs. true values $\mathcal{L}_t^{\text{true}}$ for *Cloud (i)*, in Setup A. Fig. 8[Bottom] indicates that $\hat{\mathcal{L}}_t(\{w_t\}_{t \in \mathcal{T}})$ based on this Gaussian-weight set yields a good approximation of \mathcal{L}_t . These results support the use of Gaussian weights for 4D CT of cloud LWC (Eqs. 3,4 above).

References

- [1] Austin Abrams, Kyla Miskell, and Robert Pless. The episolar constraint: Monocular shape from shadow correspondence. In *Proc. IEEE CVPR*, pages 1407–1414, 2013. 2
- [2] NASA Federal agency. *NASA Earth Data Site*. <https://worldview.earthdata.nasa.gov/>. 2
- [3] Richard P Brent. *Algorithms for minimization without derivatives*. Courier, 2013. 2
- [4] Paul Bromiley. Products and convolutions of Gaussian probability density functions. *Tina-Vision Memo*, 3(4):1, 2003. 6
- [5] Howard R Gordon, James W Brown, and Robert H Evans. Exact Rayleigh scattering calculations for use with the Nimbus-7 coastal zone color scanner. *Applied Optics*, 27(5):862–871, 1988. 2
- [6] Michael Hatzitheodorou and John R Kender. An optimal algorithm for the derivation of shape from shadows. In *Proc. IEEE CVPR*, pages 486–487, 1988. 2
- [7] Aviad Levis, Yoav Y Schechner, Amit Aides, and Anthony B Davis. Airborne three-dimensional cloud tomography. In *Proc. IEEE ICCV*, pages 3379–3387, 2015. 2, 4, 5
- [8] Gregoris Liasis and Stavros Stavrou. Satellite images analysis for shadow detection and building height estimation. *ISPRS Journal of Photogrammetry and Remote Sensing*, 119:437–450, 2016. 2
- [9] Tamar Loeb, Aviad Levis, Vadim Holodovsky, and Yoav Y Schechner. Monotonicity prior for cloud tomography. In *Proc. ECCV*, pages 24–29, 2020. 4
- [10] Roi Ronen. *4D Cloud Scattering Tomography. 2021*. Available online. <https://github.com/ronenroi/4D-Cloud-Scattering-Tomography>. 5
- [11] The SciPy community. *SciPy. 2020*. Available online. https://docs.scipy.org/doc/scipy/reference/generated/scipy.optimize.minimize_scalar.html. 2
- [12] Flavio R Velasco. Thresholding using the ISODATA clustering algorithm. Technical report, Univ. of Maryland College Park, Computer Science Center, 1979. 2
- [13] Menghua Wang. A refinement for the Rayleigh radiance computation with variation of the atmospheric pressure. *International Journal of Remote Sensing*, 26(24):5651–5663, 2005. 2